Cell Reports

Report

Paradoxical hyperexcitability from $Na_V1.2$ sodium channel loss in neocortical pyramidal cells

Graphical abstract

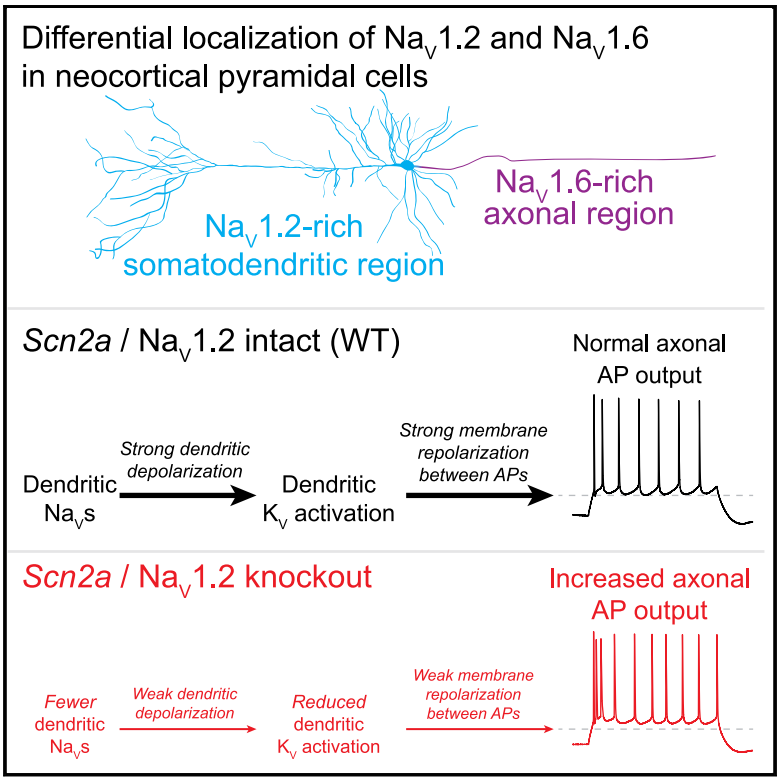

Highlights

- Conditional deletion of $Na_V1.2$ channels increases action potential (AP) excitability
- $Na_V1.2$ regulates somatodendritc excitability, and $Na_V1.6$ regulates axonal action potential initiation
- Lack of $Na_V1.2$ channels impairs AP repolarization by reducing K_V activation
- Reduced K_V-mediated AP after hyperpolarization increases AP output

Authors

Perry W.E. Spratt, Ryan P.D. Alexander, Roy Ben-Shalom, ..., Caroline M. Keeshen, Stephan J. Sanders, Kevin J. Bender

Correspondence

kevin.bender@ucsf.edu

In brief

Loss of sodium channels in individual neurons is expected to reduce neuronal excitability. Spratt and colleagues show that loss of *Scn2a*-encoded $Na_V1.2$ channels in mouse prefrontal pyramidal cells can paradoxically increase excitability due to $Na_V1.2$'s distinct role in regulating somatodendritic excitability, independent of action potential electrogenesis in the axon.

Spratt et al., 2021, Cell Reports *36*, 109483
August 3, 2021
https://doi.org/10.1016/j.celrep.2021.109483

CellPress

Cell Reports

CellPress
OPEN ACCESS

Report

Paradoxical hyperexcitability from $Na_V1.2$ sodium channel loss in neocortical pyramidal cells

Perry W.E. Spratt,[1] Ryan P.D. Alexander,[2] Roy Ben-Shalom,[2] Atehsa Sahagun,[2] Henry Kyoung,[2] Caroline M. Keeshen,[2] Stephan J. Sanders,[3] and Kevin J. Bender[1,2,4,*]

[1]Neuroscience Graduate Program, Kavli Institute for Fundamental Neuroscience, Weill Institute for Neurosciences, University of California, San Francisco, San Francisco, CA, USA

[2]Department of Neurology, Kavli Institute for Fundamental Neuroscience, Weill Institute for Neurosciences, University of California, San Francisco, San Francisco, CA, USA

[3]Department of Psychiatry, Kavli Institute for Fundamental Neuroscience, Weill Institute for Neurosciences, University of California, San Francisco, San Francisco, CA, USA

[4]Lead contact

*Correspondence: kevin.bender@ucsf.edu

https://doi.org/10.1016/j.celrep.2021.109483

SUMMARY

Loss-of-function variants in the gene *SCN2A*, which encodes the sodium channel $Na_V1.2$, are strongly associated with autism spectrum disorder and intellectual disability. An estimated 20%–30% of children with these variants also suffer from epilepsy, with altered neuronal activity originating in neocortex, a region where $Na_V1.2$ channels are expressed predominantly in excitatory pyramidal cells. This is paradoxical, as sodium channel loss in excitatory cells would be expected to dampen neocortical activity rather than promote seizure. Here, we examined pyramidal neurons lacking $Na_V1.2$ channels and found that they were intrinsically hyperexcitable, firing high-frequency bursts of action potentials (APs) despite decrements in AP size and speed. Compartmental modeling and dynamic-clamp recordings revealed that $Na_V1.2$ loss prevented potassium channels from properly repolarizing neurons between APs, increasing overall excitability by allowing neurons to reach threshold for subsequent APs more rapidly. This cell-intrinsic mechanism may, therefore, account for why *SCN2A* loss-of-function can paradoxically promote seizure.

INTRODUCTION

Genetic variation in *SCN2A* is a major risk factor for neurodevelopmental disorders, including developmental epilepsies, autism spectrum disorder (ASD), and intellectual disability. *SCN2A* encodes $Na_V1.2$, a voltage-gated sodium channel (Na_V) that supports neuronal excitability throughout the brain, including cortical regions where it is expressed primarily in excitatory neurons (Hu et al., 2009; Spratt et al., 2019). Consistent with this expression pattern, *SCN2A* variants that enhance $Na_V1.2$ function—and, therefore, excitatory activity in cortex—are most commonly associated with epilepsy. By contrast, loss-of-function (LoF) variants that dampen or eliminate channel function are typically associated with intellectual disability and ASD (Howell et al., 2015; Sanders et al., 2018; Wolff et al., 2017). Yet, an estimated 20%–30% of children with *SCN2A* LoF variants develop epilepsy (Sanders et al., 2018). The cellular mechanisms underlying seizure in conditions where Na_V impairment is largely restricted to excitatory neurons are unknown.

Mouse models of heterozygous *Scn2a* loss ($Scn2a^{+/-}$) suggest that seizures originate in neocortical pyramidal cells (Miyamoto et al., 2019; Ogiwara et al., 2018). Electroencephalograms (EEGs) from $Scn2a^{+/-}$ mice exhibit spike-and-wave discharges characteristic of absence epilepsies at relatively low frequency (<10 events/h) (Ogiwara et al., 2018). Similar EEG patterns have been observed with conditional heterozygous expression of *Scn2a* in excitatory, but not inhibitory, neocortical neurons (Ogiwara et al., 2018). However, changes in action potential (AP) output, a feature common to many models of Na_V-channelopathy-mediated epilepsy (Goff and Goldberg, 2019; Li et al., 2020; Lopez-Santiago et al., 2017; Martin et al., 2010; Tai et al., 2014), have not been observed in mature $Scn2a^{+/-}$ pyramidal cells (Shin et al., 2019; Spratt et al., 2019).

Given the incomplete penetrance of seizure in children with *SCN2A* LoF, as well as the low rates of spike-and-wave discharges observed in $Scn2a^{+/-}$ mice, seizure-associated cellular phenotypes may be too subtle to discern in heterozygotes. In such cases, homozygous deletion may help identify cellular mechanisms disrupted by gene loss. This appears to be the case for *Scn2a* LoF conditions, as full deletion of *Scn2a* from striatally projecting layer 5b pyramidal cells alone can recapitulate spike-and-wave discharge phenotypes observed in mice heterozygous for *Scn2a* in all pyramidal cells (Miyamoto et al., 2019). Thus, understanding how complete loss of *Scn2a* in layer

5b pyramidal cells results in hyperexcitability may shed light on seizure susceptibility in general.

Here, we examined cell-autonomous features of neuronal excitability in mice with conditional deletion of *Scn2a* in prefrontal pyramidal cells. Remarkably, despite deletion of a sodium (Na) conductance, neurons were more excitable, exhibiting an increase in both overall AP number and high-frequency AP bursts. This was due to the unique function and localization of $Na_V1.2$ in pyramidal cell neuronal compartments relative to other Na_V and potassium (K) channel classes. $Na_V1.2$ was not responsible for AP initiation, a process dependent instead on $Na_V1.6$ channels in the axon initial segment (AIS) (Hu et al., 2009). Rather, $Na_V1.2$ was critical for propagating APs through the soma and dendrites and for activating voltage-gated K channels that repolarized neurons. Loss of $Na_V1.2$ resulted in increased neuronal excitability largely through a failure to properly repolarize neurons between APs, and aspects of normal excitability could be rescued by injection of $Na_V1.2$ conductance via dynamic clamp. Thus, an interplay between ion channel classes can affect electrogenesis in counterintuitive ways, highlighting the importance of considering neuronal excitability in different cellular compartments in neurodevelopmental channelopathy conditions.

RESULTS

Hyperexcitability of AP initiation from $Na_V1.2$ deletion

Though *Scn2a*$^{+/-}$ mice exhibit spike-and-wave discharge epileptiform activity (Ogiwara et al., 2018), *ex vivo* studies of *Scn2a*$^{+/-}$ pyramidal cells have yet to identify cellular mechanisms to explain such events, including possible cell-intrinsic hyperexcitability. To examine neuronal excitability in the absence of $Na_V1.2$ channels, we used a mouse line homozygous for conditional *Scn2a* knockout under Cre-recombinase control (*Scn2a*$^{fl/fl}$). AAV-EF1α-Cre-mCherry was injected unilaterally into the medial prefrontal cortex (PFC) of *Scn2a*$^{fl/fl}$ or *Scn2a*$^{+/fl}$ mice at postnatal days 28–44, and neuronal excitability was examined *ex vivo* >4 weeks after injection. $Na_V1.2$ deletion in *Scn2a*$^{fl/fl}$-injected cells was confirmed with immunofluorescent staining of $Na_V1.2$ in the AIS (Figures S1A and S1B). Whole-cell current clamp recordings were made from mCherry-positive L5b neurons in the injected hemisphere and compared to mCherry-negative neurons in the contralateral uninfected hemisphere or neurons in age-matched wild-type (WT) mice. For simplicity, neurons conditionally lacking one or both *Scn2a* alleles are termed *Scn2a*$^{+/-}$ and *Scn2a*$^{-/-}$ throughout, whereas mCherry-negative neurons from either *Scn2a*$^{+/fl}$ or *Scn2a*$^{fl/fl}$ animals are pooled and termed WT.

AP excitability was assessed with somatic current injection (Firing/Current [F/I] curves; Figures 1A and 1B). Consistent with previous work, *Scn2a*$^{+/-}$ F/I curves were no different than WT ($^{+/+}$: 3.78 ± 0.13 APs per 100 pA between 100 and 300 pA, n = 77; $^{+/-}$: 3.54 ± 0.21, n = 40, p = 0.2); however, *Scn2a*$^{-/-}$ neurons had a pronounced increase in F/I slope (Figure 1B; $^{-/-}$: 4.55 ± 0.13, n = 60; $^{+/+}$ versus $^{-/-}$ and $^{+/-}$ versus $^{-/-}$, p < 0.001). This was due to an increase in both the number of APs generated during high-frequency bursts at current onset as well as the steady-state AP number closer to current offset in *Scn2a*$^{-/-}$ neurons (Figure 1B).

To better understand how neuronal excitability is affected by *Scn2a* loss, we examined the expression and function of $Na_V1.6$. In contrast to $Na_V1.2$, which is localized primarily to somatodendritic compartments in mature neocortical pyramidal cells, $Na_V1.6$ is expressed at high levels in the axon and mediates the initiation and propagation of orthodromic APs (Hallermann et al., 2012; Hu et al., 2009; Li et al., 2014; Spratt et al., 2019). To assay $Na_V1.6$ function, we first measured persistent Na_V currents, which reflect the recruitment of low-threshold AIS-localized Na_Vs (Taddese and Bean, 2002). We also examined the intensity of $Na_V1.6$ immunofluorescent staining in the AIS in infected versus uninfected hemispheres. In both cases, modest increases in channel function/expression were evident: median persistent currents were increased by 18% for steps from −90 to −60 mV in *Scn2a*$^{-/-}$ neurons (Figures S1G and S1H), and $Na_V1.6$ fluorescent intensity, normalized to its AIS scaffolding partner, ankyrin-G, was increased by 13% (Figures S1A–S1D).

We examined other aspects of neuronal excitability, including the resting membrane potential, input resistance, and K current. Resting membrane potential did not differ with *Scn2a* expression level ($^{+/+}$: 74.9 ± 0.4 mV, n = 92; $^{+/-}$: 73.8 ± 1.3, n = 47; $^{-/-}$: 73.9 ± 0.6, n = 47, p = 0.177). As with previous comparisons between WT and *Scn2a*$^{+/-}$ cells (Spratt et al., 2019), whole-cell K currents were not different in *Scn2a*$^{-/-}$ cells (Figures S1I and S1J), though these currents were quite large, and the transient component displayed little voltage dependence, indicative of poor voltage clamp. Therefore, we next examined the amplitude and kinetics of transient and delayed K currents in nucleated patches pulled from *Scn2a*$^{+/+}$ and *Scn2a*$^{-/-}$ cells. The voltages of half activation for both transient and delayed currents were no different across groups (transient, $^{+/+}$: −9.7 ± 3.3 mV, n = 11; $^{-/-}$: −6.5 ± 4.7 mV, n = 11; p = 0.2, Mann-Whitney; delayed, $^{+/+}$: −16.2 ± 4.0 mV; $^{-/-}$: −22.1 ± 6.5 mV; p = 0.7, Mann-Whitney). Similarly, current amplitude and kinetics of activation and inactivation of transient currents were not affected by *Scn2a* knockout (Figures S1K and S1L). Input resistance, however, was higher in *Scn2a*$^{-/-}$ cells, potentially contributing to increased excitability. To test this, we compared F/I slope to neuronal input resistance (Figures S1M and S1N). While a modest correlation was observed in WT cells (R^2 = 0.14), no such correlation was observed in *Scn2a*$^{+/-}$ or *Scn2a*$^{-/-}$ cells (R^2 = 0.006 and 0.004, respectively; p > 0.5), where slopes were higher even in cells with low input resistance. Overall, these data suggest that increased AP output is unlikely to be explained by changes in K-channel function or modest changes in intrinsic membrane resistance alone.

In light of these observations, we predicted that axonal AP propagation, supported by $Na_V1.6$, was likely to be intact, even with $Na_V1.2$ loss. To test this, we made simultaneous whole-cell recordings from the soma and an axonal bleb formed as the primary axon exits the slice surface. Blebs were identified at various distances from the axon hillock in both WT and *Scn2a*$^{-/-}$ cells. AP conduction delays between soma and bleb were unaltered when accounting for axon length (Figures 1C and 1D; conduction velocity, $^{+/+}$: 1.26 ± 0.29 m/s, n = 7; $^{-/-}$: 1.21 ± 0.36, n = 5, p = 0.8, Mann-Whitney). Next, we confirmed that APs could propagate to neurotransmitter release sites by measuring AP-evoked calcium transients in axonal boutons using two-photon microscopy. APs reliably generated calcium

CellPress
OPEN ACCESS

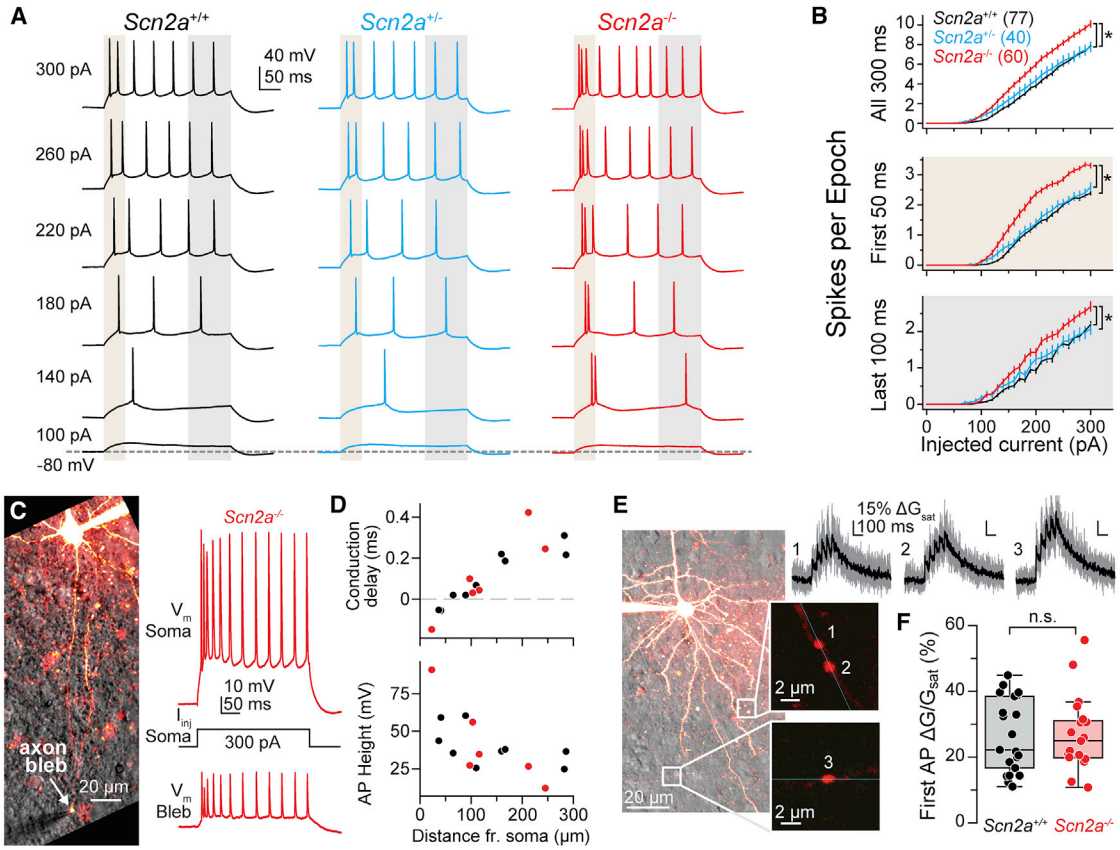

Figure 1. *Scn2a* knockout increases AP excitability, with intact axonal propagation

(A) APs (spikes) per 300-ms stimulation epoch for each current amplitude in *Scn2a*$^{+/+}$ (black), *Scn2a*$^{+/-}$ (cyan), and *Scn2a*$^{-/-}$ (red) cells. Brown and gray areas highlight first 50 ms and last 100 ms of epoch, respectively.

(B) APs versus current for 3 *Scn2a* conditions, color coded as in (A). Bars are mean ± SEM; n = 77 WT, 40 *Scn2a*$^{+/-}$, 60 *Scn2a*$^{-/-}$ cells. Top: entire 300-ms epoch. Middle: first 50 ms. Bottom: last 100 ms. Asterisk indicates F/I slope between 100 and 300 pA. $p < 0.01$, Kruskal-Wallis test. Scale bar: 20 µm.

(C) Scanning differential contrast and two-photon fluorescent image of simultaneous recordings in a *Scn2a*$^{-/-}$ pyramidal neuron of APs evoked from soma and recorded at axon bleb 212 µm from axon hillock.

(D) Conduction delay of AP threshold between soma and bleb in each recording versus axon length and AP amplitude in bleb in *Scn2a*$^{+/+}$ (black, n = 9) and *Scn2a*$^{-/-}$ (red, n = 6) cells.

(E) Scanning differential contrast and two-photon fluorescent image detailing bouton scan sites for AP-evoked calcium imaging of a *Scn2a*$^{-/-}$ neuron (insets). Responses to burst of five APs at boutons 1–3 are shown as average (black) overlaid on single trials (gray, 10 trials total).

(F) First AP amplitude is no different between *Scn2a*$^{+/+}$ (n = 21) and *Scn2a*$^{-/-}$ (n = 19) cells. Scale bar: 20 µm; inset: 2 µm.

transients in *Scn2a*$^{-/-}$ boutons, with no differences in transient amplitude compared to WT (Figure 1E). These data indicate that axonal AP propagation is intact in *Scn2a*$^{-/-}$ cells and is supported by $Na_V1.6$.

Hypoexcitability of dendritic AP backpropagation from $Na_V1.2$ deletion

Heterozygous loss of $Na_V1.2$ impairs somatodendritic excitability in mature neocortical pyramidal cells, affecting both AP waveform recordings at the soma and AP-evoked calcium signaling in dendrites (Spratt et al., 2019). To determine the effects of full $Na_V1.2$ deletion, we examined AP waveform at the soma using phase-plane analysis, which compares the rate of change in voltage during APs to the voltage (Jenerick, 1963). These plots help reveal different aspects of AP initiation, including a sharp kink at AP threshold and two distinct components of the rising phase of an AP that reflect the initial activation of AIS Na_Vs and subsequent recruitment of somatodendritic Na_Vs (Figures 2B and 2C). AP threshold was not altered by heterozygous or homozygous loss of *Scn2a* (Figures 2A–2D). Similarly, the AIS-associated component of the AP rising phase was unaltered (Figures 2C and 2E). Backpropagation of the AIS-evoked AP into the soma appeared to be reliable, as assayed by evoking APs from a whole-cell recording of a near-AIS axonal bleb while monitoring somatic voltage (Figure S2). Together, these data are consistent with normal AIS AP initiation, mediated by $Na_V1.6$ channels.

While axonal aspects of AP initiation were not affected by *Scn2a* loss, somatodendritic features of AP initiation were increasingly impaired as *Scn2a* expression was reduced by 50% (heterozygote) or 100% (conditional knockout). Peak AP height and depolarization speed both reflect engagement of

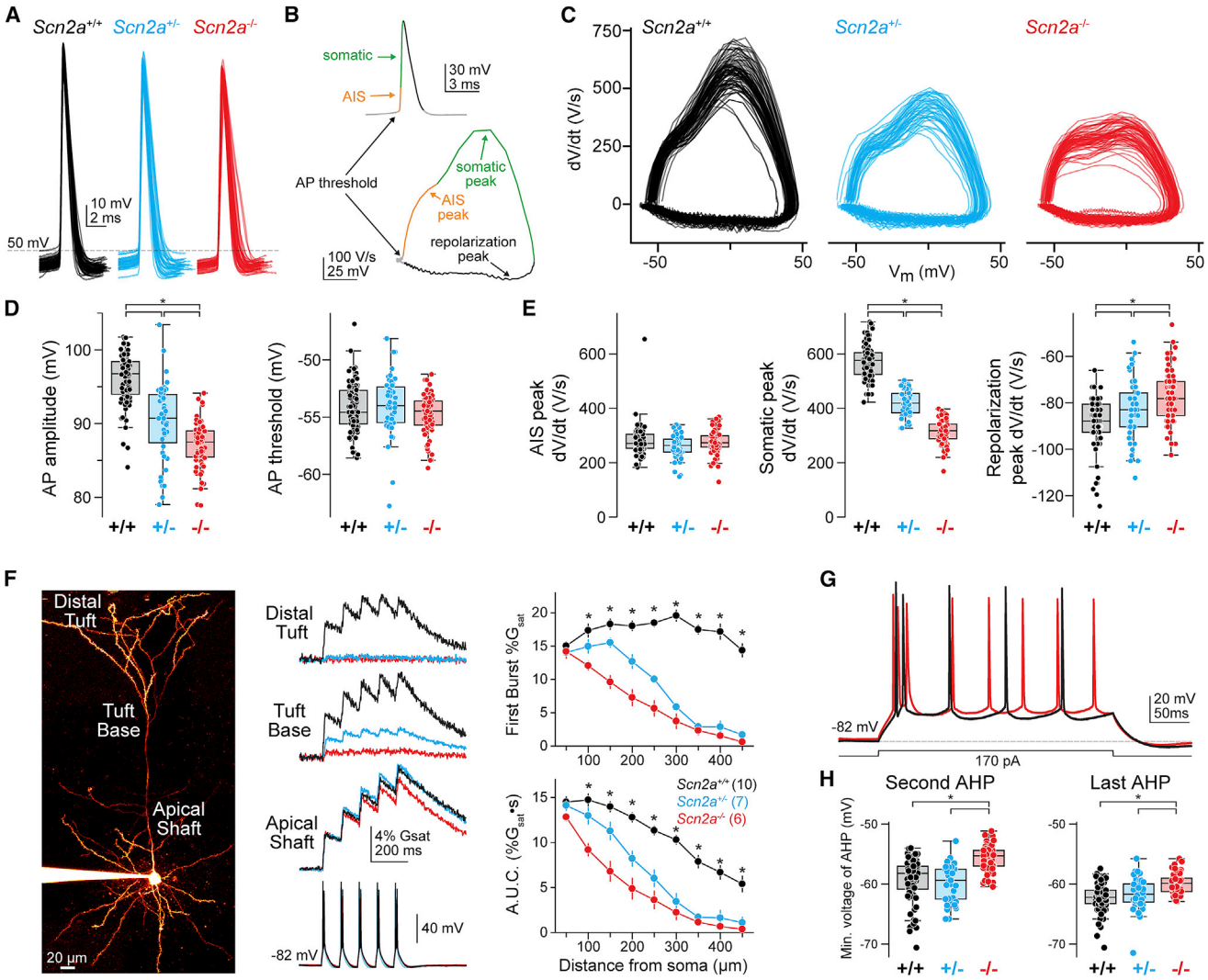

Figure 2. *Scn2a* knockout impairs somatodendritic excitability

(A) Rheobase AP waveform from all neurons. Note reduction in AP height with loss of $Na_V1.2$.

(B) AP plotted as voltage versus time (top) and dV/dt versus voltage (phase-plane, bottom). Different phases of the AP are color-coded across panels to indicate different phases of the AP corresponding to initiation of AP in AIS, the soma, and peak repolarization.

(C) Phase plane of data shown in (A).

(D) Amplitude and threshold of APs at rheobase. Circles are single cells. Boxplots are median, quartiles, and 90% tails. Data color-coded as in (A). *$p < 0.001$, Kruskal-Wallis test.

(E) Peak of AIS and somatic components of the rising phase of the AP and minimum of the falling phase of the AP. *$p < 0.001$, Kruskal-Wallis test.

(F) Left: morphology of imaged neuron. Middle: 2-photon calcium imaging of AP-evoked calcium transients throughout apical tuft dendrites in *Scn2a*$^{+/+}$ (black, n = 10), *Scn2a*$^{+/-}$ (cyan, n = 7), and *Scn2a*$^{-/-}$ (red, n = 6) cells. Right: transient amplitude shown for first of five bursts (top) and area under the curve from stimulus onset to stimulus offset +100 ms (bottom). Circles and bars are means ± SEM. *$p < 0.01$, Kruskal-Wallis test. Scale bar: 20 µm.

(G) Overlaid AP response to 170-pA current injection in *Scn2a*$^{+/+}$ (black) and *Scn2a*$^{-/-}$ (red) cell. Note difference in AHP amplitude.

(H) AHP amplitude of the second (left) and final (right) interspike intervals during spike trains elicited by 300-pA current injection. *$p < 0.001$, Kruskal-Wallis test. Note that n is the same as in Figure 1 for (A)–(E) and (H).

somatodendritic Na_Vs. These features were smaller than WT in *Scn2a*$^{+/-}$ cells and smaller still in *Scn2a*$^{-/-}$ cells (Figures 2A–2E). Similarly, AP-evoked dendritic calcium transients, which reflect local dendritic activation of voltage-gated calcium channels, were impaired markedly in *Scn2a*$^{-/-}$ cells (Figure 2F). Thus, axonal and dendritic function are differentially affected by $Na_V1.2$ deletion, with increased excitability in measures of axonal AP output and decreased excitability in measures of dendritic function.

$Na_V1.2$ deletion affects K-channel-mediated AP repolarization

Just as membrane potential preceding an AP affects AP threshold (Azouz and Gray, 2000; Bender and Trussell, 2009;

CellPress
OPEN ACCESS

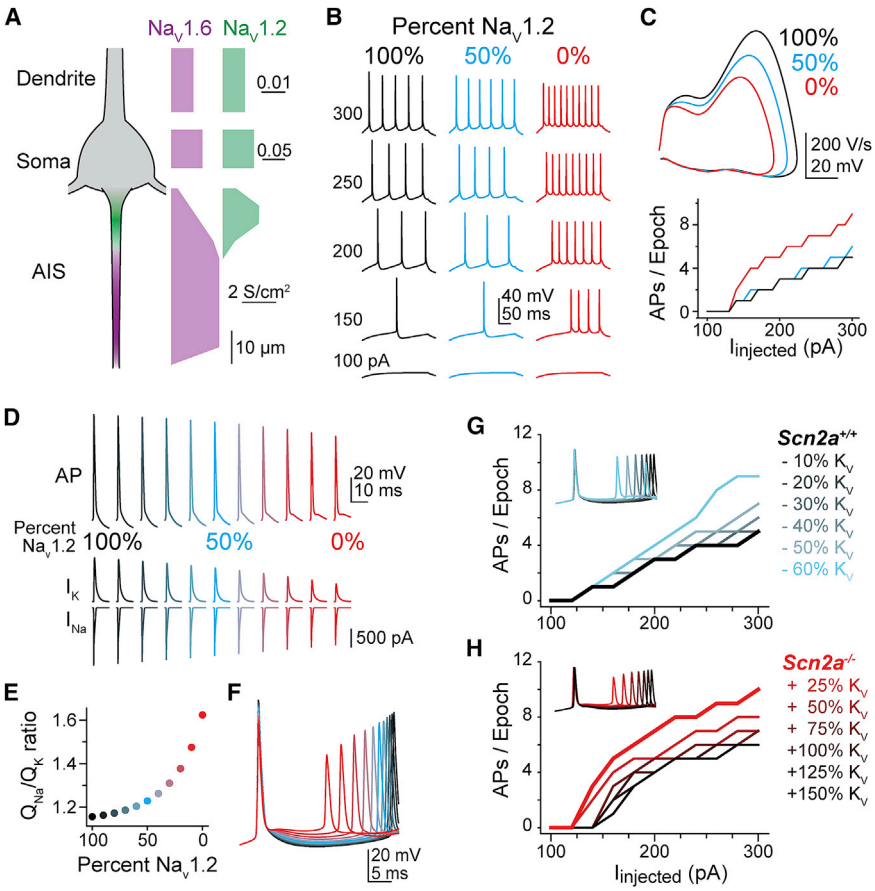

Figure 3. *Scn2a* loss in dendrites increases AP excitability in compartmental models

(A) Compartmental model of layer 5 pyramidal cell with Na$_V$1.2 and Na$_V$1.6 distributed in the AIS soma and dendrites as shown. Purple and green for Na$_V$1.2 and Na$_V$1.6 show relative densities in dendrite, soma, and AIS in model. Note different scale bars for each compartment.

(B) Firing patterns of models in which Na$_V$1.2 is reduced to 50% or 0% in all compartments. Data are color-coded as in Figures 1 and 2.

(C) Phase planes and F/I curves for each model. Note that increase in F/I is appreciable only in *Scn2a*$^{-/-}$ conditions.

(D) APs elicited by 350-pA current and underlying whole-cell Na and K currents with progressive loss of Na$_V$1.2.

(E) Charge transfer (Q) ratio (Na/K) for each AP as a function of Na$_V$1.2 density. 100% is WT levels, and 0% is *Scn2a*$^{-/-}$.

(F) Timing of first APs in conditions noted in (D) and (E) (identical color coding). Note depolarization of AHP and advanced AP2 timing with Na$_V$1.2 loss.

(G) Reducing K conductance in WT model recapitulates hyperexcitability observed in *Scn2a*$^{-/-}$ cells due to depolarization of AHP (inset).

(H) Increasing K conductance in *Scn2a*$^{-/-}$ model reduces excitability, in part by delaying AP timing (inset).

Hu et al., 2009; Kole et al., 2007; Uebachs et al., 2006), the amplitude of an AP affects its repolarization by altering K-channel driving force. Indeed, in *Scn2a*$^{-/-}$ cells, where AP height is reduced by 9 mV, AP repolarization speed was reduced 12% (Figure 2E; $^{+/+}$: −88.69 ± 1.14 mV, n = 91; $^{-/-}$: −77.38 ± 1.35, n = 67), and membrane potential between APs (e.g., afterhyperpolarization [AHP]) was more depolarized than in WT cells throughout spike trains (Figures 2G and 2H; second AHP with 300-pA current injection, $^{+/+}$: −59.4 ± 0.4 mV, n = 77; $^{-/-}$: −55.7 ± 0.3, n = 56, p < 0.001; final AHP, $^{+/+}$: −62.3 ± 0.3, n = 77; $^{-/-}$: −60.0 ± 0.2, n = 56, p < 0.001). This may contribute to hyperexcitability observed in cells with Na$_V$1.2 deletion by allowing neurons to reach threshold for subsequent APs more quickly.

To better understand the role of these effects in neuronal excitability, we examined how Na$_V$1.2 loss and modest increases in Na$_V$1.6 affected repetitive AP activity in compartmental models, with Na$_V$1.6 and Na$_V$1.2 distributed as previously described (Ben-Shalom et al., 2017; Spratt et al., 2019). We began by isolating increases in Na$_V$1.6 alone to determine its contribution to AP waveform and repetitive activity. Na$_V$1.6 density was increased by 20% and 50%, matching or exceeding increased Na$_V$1.6 staining and persistent Na current observed in *Scn2a*$^{-/-}$ cells (Figure S3A). As expected from increasing Na$_V$ density, the speed of AP depolarization was increased; however, increasing Na$_V$1.6 density reduced, rather than increased, the frequency of subsequent APs. Thus, modest increases in Na$_V$1.6 appear unable to account for hyperexcitability observed in *Scn2a*$^{-/-}$ conditions. Instead, models were able to capture several aspects present in empirical data simply by lowering Na$_V$1.2 density. Excitability increased modestly at 50% Na$_V$1.2 density but increased dramatically with complete Na$_V$1.2 removal (Figures 3B and 3C), mirroring effects observed in *Scn2a*$^{+/-}$ and *Scn2a*$^{-/-}$ conditions (Figure 1). Effects on AP output were similar whether or not Na$_V$1.6 density was increased, suggesting that Na$_V$1.6 density has little effect on repetitive activity. Similarly, increasing input resistance in models did not alter excitability in ways that mimicked *Scn2a*$^{-/-}$ conditions (Figure S3C).

As in neurons, effects on repetitive AP activity correlated with changes in AP height and K-channel engagement. We therefore asked how K channels activated during AP repolarization were affected by progressive removal of Na$_V$1.2 from models. Interestingly, as Na$_V$1.2 density was reduced, the relationship between Na$_V$ and K-channel current generated during an AP was exponential rather than linear. At 50% Na$_V$1.2 density, the ratio of the charge transfer (Q) of Na versus K current during the AP was only 6% higher than in 100% Na$_V$1.2 density conditions. By contrast, this ratio was 40% higher when Na$_V$1.2 was deleted completely (Figures 3D–3F). This exponential relationship may account for why *Scn2a* heterozygotes have F/I curves that are comparable to WTs, whereas *Scn2a*$^{-/-}$ cells are markedly hyperexcitable.

This modeling suggests that the interplay between Na$_V$1.2 and voltage-gated K channels, rather than changes in Na$_V$1.6

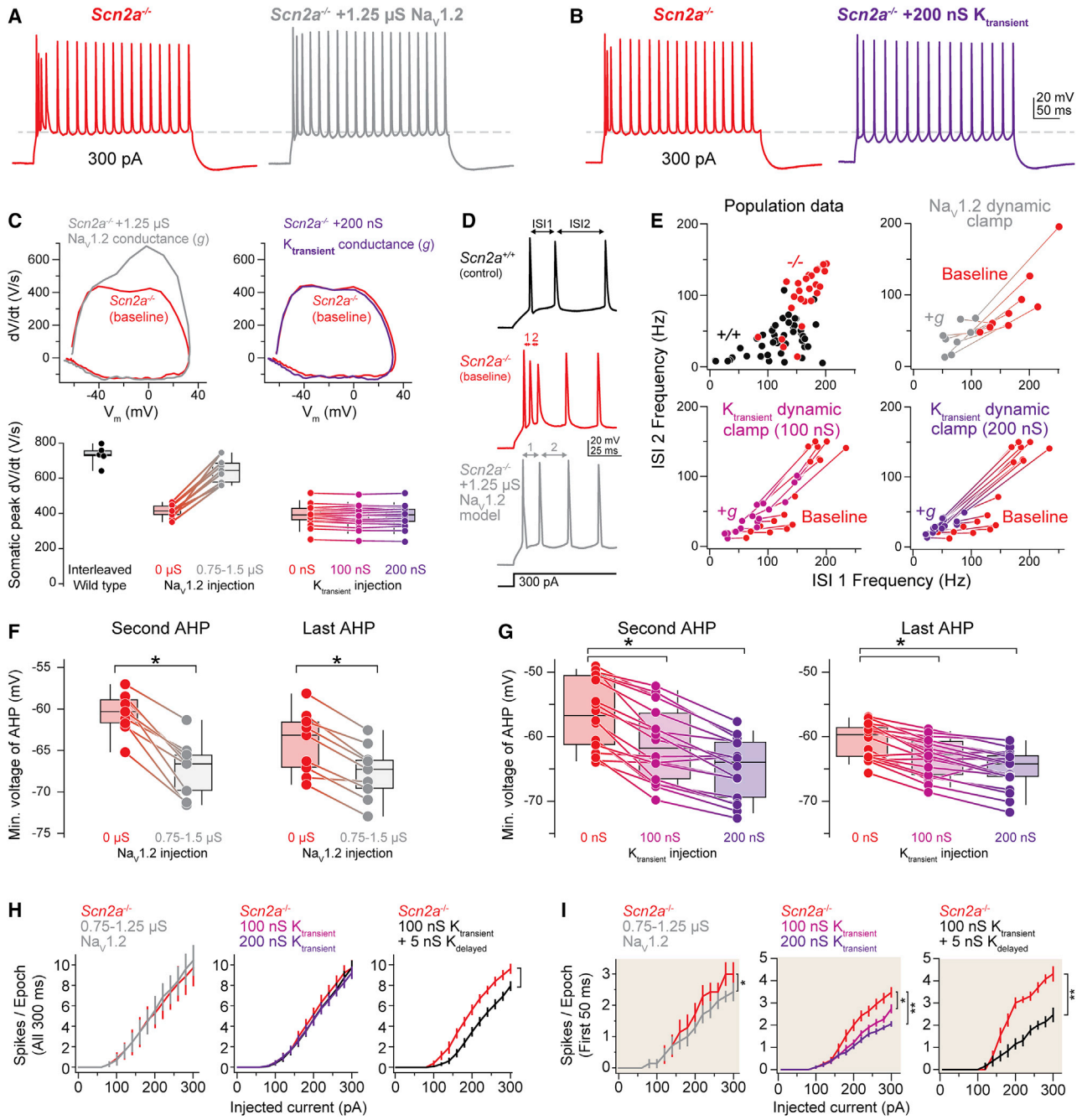

Figure 4. Dynamic-clamp injection of $Na_V1.2$ or $K_{transient}$ conductance rescues excitability

(A) AP firing response to 300-pA, 300-ms current before (red) and after (gray) injection of 1.25 µS $Na_V1.2$ conductance via somatic recording electrode. Dashed line is aligned to last AHP in baseline conditions.

(B) As in (A), but for 200 nS of $K_{transient}$. Baseline is in red, and $K_{transient}$ injection is in purple.

(C) Top: phase planes of first AP for each condition in (A) and (B). Bottom: summary data for interleaved WT cells (n = 5) in identical recording conditions and for all *Scn2a*$^{-/-}$ cells with $Na_V1.2$ (n = 9) or $K_V1.2$ (n = 18) conductance injection. Circles are single cells with lines connecting paired data. n applies to all panels.

(D) Highlight of timing of first three APs in WT and *Scn2a*$^{-/-}$ before and after $Na_V1.2$ conductance injection. Inter-spike intervals (ISIs) for APs 1–2 and 2–3 are plotted in (E).

(E) Top left: ISI1 versus ISI2 at 300-pA current injection for all WT (black) and *Scn2a*$^{-/-}$ (red) cells in population in Figure 1. Other panels show change in ISIs from *Scn2a*$^{-/-}$ baseline (red) after conductance injection (other colors). Lines connect values from the same cell.

(F) Minimum voltage between APs (e.g., AHP) between APs 2 and 3 and the penultimate and last APs for 300-pA stimulus injection before and after $Na_V1.2$ conductance injection. Data shown as in (C). *p < 0.01, Wilcoxon signed rank test.

(legend continued on next page)

density, is the primary driver of hyperexcitability in *Scn2a*$^{-/-}$ cells. Consistent with this, increased K-channel density in *Scn2a*$^{-/-}$ models reduces excitability, while reduced K-channel density in *Scn2a*$^{+/+}$ models increases excitability (Figures 3G and 3H). Together, these models predict that injection of conductances that mimic $Na_V1.2$ engaged during AP depolarization, or K channels engaged during AP repolarization, should restore features of WT excitability in *Scn2a*$^{-/-}$ cells. We tested this using somatic dynamic-clamp injection of $Na_V1.2$-like or transient K ($K_{transient}$) conductances into *Scn2a*$^{-/-}$ cells (Figures 4A and 4B). For $Na_V1.2$ conductance injection, injection amplitude was adjusted to restore AP peak dV/dt to 88% of WT levels in these recording conditions, which was the maximum restoration attainable without inducing feedback within the amplifier circuitry ($^{+/+}$: 732 ± 26 V/s, n = 5; $^{-/-}$ baseline: 412 ± 12; post-0.75–1.5-μS injection: 646 ± 24, n = 9). $K_{transient}$ conductance injection, as expected, had no effect on peak dV/dt. We therefore examined two different injection intensities in each cell (100–200 nS), as these appeared to encompass a range of excitability effects similar to $Na_V1.2$ conductance injection.

Scn2a$^{-/-}$ cells often fire high-frequency bursts at current onset and have AHPs that are more depolarized than observed in WT cells (Figures 1A, 1B, and 2G). Injection of either $Na_V1.2$- or $K_{transient}$-like conductances suppressed burst generation, as assayed by the changes in instantaneous frequencies of APs 1–2 and 2–3 within spike trains (Figures 4D and 4E). Similarly, AHP amplitudes were hyperpolarized by injection of either $Na_V1.2$ or $K_{transient}$ conductances (Figures 4F and 4G). Despite restoring these aspects of neuronal excitability to WT-like levels, and despite observing changes in the first 50 ms of F/I curves, overall F/I curves (300-ms epochs) were largely unaffected by $Na_V1.2$ conductance injection (Figures 4H and 4I). This may be due to the limited effect of transient conductances, including $Na_V1.2$, on axonal and dendritic membrane potential, due to difficulties in rapidly charging membranes more distal to the injection electrode, akin to space-clamp errors in voltage-clamp recordings (Williams and Mitchell, 2008). We tested this idea *in silico* by examining F/I curves in cases where $Na_V1.2$ was rescued only in the soma and/or proximal AIS compared to cases where $Na_V1.2$ was restored in dendritic compartments (Figure S4). As in our dynamic-clamp experiments, we found that restoration just in the soma or the AIS had little effect on overall F/I curves, even when $Na_V1.2$ density was restored to 80%–90% of WT levels (e.g., similar to dynamic-clamp rescue of dV/dt).

In addition to space-clamp issues, $K_{transient}$ conductances are subject to voltage-dependent inactivation (Korngreen and Sakmann, 2000), which would reduce conductance amplitude related to APs that occur later in stimulus epochs. Consistent with this, F/I curves were suppressed by $K_{transient}$ injection within the first 50 ms of stimulus onset, but not when the entire 300-ms epoch was examined (Figures 4H and 4I). Thus, injection of $K_{transient}$ conductances alone may not mimic how real dendrites respond to $Na_V1.2$-mediated excitability. Indeed, neocortical dendrites express a complement of transient and sustained K channels (Harnett et al., 2013; Korngreen and Sakmann, 2000). We therefore paired $K_{transient}$ conductance injection with a delayed, non-inactivating K current. Under these conditions, the F/I curve in *Scn2a*$^{-/-}$ cells could be suppressed to WT-like levels in both the first 50 ms and the entire 300-ms epoch (Figures 4H and 4I). Together, these data suggest that interactions between $Na_V1.2$ and K channels in both the soma and dendrites are critical in regulating overall pyramidal cell excitability and highlight the importance of $Na_V1.2$ in somatodendritic excitability.

DISCUSSION

Neurodevelopmental epilepsies are associated with genetic variation in all three central-nervous-system-localized Na_Vs. For *SCN1A*, epilepsy stems almost exclusively from LoF variants that impair channel function, due to resulting deficits in inhibitory interneuron excitability and circuit disinhibition (Goff and Goldberg, 2019; Tai et al., 2014). For *SCN8A*, epilepsy manifests largely from gain-of-function (GoF) variants that produce neuronal hyperexcitability in excitatory networks (Lopez-Santiago et al., 2017). *SCN2A* is unique in that both GoF and LoF are associated with seizure. For GoF *SCN2A* variants, where the age of seizure onset is within days to months of birth, the underlying mechanisms appear related to hyperexcitability in glutamatergic neuronal axons (Gazina et al., 2015; Sanders et al., 2018). For LoF conditions, where the age of seizure onset is typically after 12 months of life (Brunklaus et al., 2020), the underlying cellular mechanisms have been less clear. Here, we identified a candidate mechanism for such hyperexcitability: the interplay between Na and K-channel electrogenesis and the resulting increased excitability due to a failure to properly repolarize neurons between APs.

Several lines of evidence support this hypothesis. First, *in vivo* data from mouse show that aberrant EEG signatures in *Scn2a* LoF conditions arise from dysfunction in neocortical pyramidal cells (Miyamoto et al., 2019; Ogiwara et al., 2018) and that conditional heterozygous expression of *Scn2a* in neocortical inhibitory neurons has no effect on EEG patterns (Ogiwara et al., 2018). Furthermore, complete deletion of *Scn2a* only from striatally projecting layer 5b pyramidal cells has similar effects on EEG activity. Together, this indicates that dysfunction in layer 5 pyramidal cell physiology is likely causal to seizure phenotypes.

Second, the timing of seizure onset in LoF conditions corresponds with a developmental switch from $Na_V1.2$ to $Na_V1.6$ in the distal AIS (Gazina et al., 2015; Hu et al., 2009; Spratt et al., 2019). Before this switch, *SCN2A* LoF would impair AP electrogenesis. But after this switch, $Na_V1.2$ has no role in AP initiation. Indeed, both AP threshold and the AIS component of the AP waveform are unaffected in conditional *Scn2a* heterozygous or homozygous knockout neurons (Figure 2). Instead, $Na_V1.2$ becomes critical for somatodendritic electrogenesis, and we

(G) As in F, but for injection of 100 and 200 nS of $K_{transient}$.
(H) Baseline versus dynamic-clamp injection compared in all cases for entire 300-ms epoch. Data are color-coded as noted in above panels. Bars are mean ± SEM. *p < 0.05, **p < 0.01 for changes in slope between 100 and 300 pA, Wilcoxon signed-rank test. n = 13 for $K_{transient}$ + $K_{delayed}$.
(I) As in (H), but for first 50 ms of stimulus.

show here that progressive loss of $Na_V1.2$ in neocortical dendrites affects AP repolarization, advancing the timing of subsequent APs. This separation of roles for different Na_V genes—with $Na_V1.6$ and $Na_V1.2$ governing axonal and dendritic electrogenesis, respectively—establishes, to our knowledge, the only condition in which LoF in a Na_V could result in AP hyperexcitability. By contrast, LoF in *SCN1A* or *SCN8A* both result in hypoexcitability, as these channels remain localized to the AIS (Katz et al., 2018; Makinson et al., 2017; Ogiwara et al., 2007).

Given these observations, why is seizure associated with only an estimated 20%–30% of patients with *SCN2A* LoF variants? Moreover, if seizure is occurring on a heterozygous background in children and can be detected at low frequency in EEG from heterozygous *Scn2a* mice, why is neuronal hyperexcitability observable only in neurons with complete *Scn2a* deletion? A possible explanation comes from our neuronal simulations, where we noted an exponential, rather than linear, relationship in the charge transfer ratio of Na and K with progressive loss of $Na_V1.2$ channels. This ratio increases only slightly from 100% to 50% $Na_V1.2$ conditions, but then increases dramatically after 50% loss. Consistent with this, a gene-trap approach that reduces *Scn2a* expression by ~75% also results in neuronal hyperexcitability (Zhang et al., 2021).

In this way, heterozygous *SCN2A* loss appears to lie at an inflection point of the curve where other aspects of neuronal excitability, perhaps encoded by common genetic variation in the population or due to variation of gene expression levels during development, could promote or protect from seizure. It is well established that common genetic variants play a major role in a range of neurodevelopmental disorders, including epilepsy (Leu et al., 2019; Speed et al., 2014) and ASD (Gaugler et al., 2014). Furthermore, genetic background can affect seizure severity in murine epilepsy models (Gu et al., 2020; Kang et al., 2018), including *Scn2a*$^{+/-}$ mice, in which aberrant EEG signals can be observed on a pure C57BL/6J background but not on mixed backgrounds (Mishra et al., 2017). Based on this, one prediction is that seizure frequency or severity should be higher in children with protein truncating variants than in those with LoF missense variants that temper, rather than eliminate, channel function. Testing this would require deep genotype-phenotype analysis of a large number of *SCN2A* variants in parallel with biophysical characterization and predicted effects on neuronal excitability in neuronal models (Ben-Shalom et al., 2017; Wolff et al., 2017;(Thompson et al., 2020)), controlling for symptom-based ascertainment.

In addition to genetic background, it is possible that neuronal excitability may be affected by *Scn2a*-loss-induced changes in the function of other ion channels. Indeed, lifelong reductions in *Scn2a* expression by 75% are associated with an increase in input resistance and changes in the expression of several genes encoding or associated with K channels (Zhang et al., 2021). In our experiments using conditional deletion, we did not observe changes in K-channel function, assayed with either whole cell or nucleated patch voltage-clamp (Figure S1); however, it remains possible that K-channel function was altered in more distal dendritic regions that were not sampled in these experiments. Furthermore, we noted small changes in input resistance and $Na_V1.6$ function with *Scn2a* knockout. In pyramidal cells, these changes do not appear to account for increased overall excitability (Figure S3); however, similar changes in other cell classes with differential distribution of Na and K channels may have other effects.

Loss of $Na_V1.2$ has dual effects: decreasing somatodendritic excitability and, paradoxically, increasing overall AP output. While the former is a direct consequence of the loss of Na_V-mediated excitability in somatodendritic compartments, we show that the latter is more indirect. By decreasing overall depolarization during an AP in somatodendritic regions, loss of $Na_V1.2$ reduces the activation of K channels, in turn altering AHP amplitude. This increases overall firing rate, as neurons can then reach threshold for subsequent APs more quickly. This contrasts with other mechanisms by which K channels support high-frequency firing. For example, K_V3 channels can be critical for generating high-frequency firing by promoting rapid repolarization, allowing Na_Vs to recover from inactivation during repetitive activity (Erisir et al., 1999; Kaczmarek and Zhang, 2017; Lau et al., 2000; Macica et al., 2003; Zagha et al., 2008). These types of interactions between K_Vs and Na_Vs may account for aspects of hyperexcitability associated with GoF variants in K channels (Niday and Tzingounis, 2018).

Considerations for genetic epilepsies

Considerable effort has been made toward understanding the cells and circuits that are etiological to seizure in multiple genetic epilepsies (Feng et al., 2019). Epilepsy associated with *SCN2A* LoF highlights the need for considering not only the cell types and circuits important for seizure, but also the subcellular distribution of associated proteins and their interactions within that subcellular ion channel network (Poolos and Johnston, 2012). Work here highlights how further blockade of Na_Vs with Na_V-blocking anti-seizure medications—already counter-indicated in *SCN2A* LoF cases—may increase seizure burden. Furthermore, this work identifies potential candidates for future therapeutic development. For example, development of activators of K channels preferentially localized to the somatodendritic domain may help counteract the loss of $Na_V1.2$ (Guan et al., 2007). Because of the exponential relationship between reduced $Na_V1.2$ function and neuronal hyperexcitability, even modest changes in K-channel function could have profound benefits for seizure control. Whether similar interactions occur with other epilepsy-associated genes (e.g., *KCNQ2/3*, *SCN1A*) remains largely unexplored. Such studies could help identify novel approaches to treating such disorders.

STAR★METHODS

Detailed methods are provided in the online version of this paper and include the following:

- KEY RESOURCES TABLE
- RESOURCE AVAILABILITY
  - Lead contact
  - Materials availability
  - Data and code availability
- EXPERIMENTAL MODEL AND SUBJECT DETAILS
- METHOD DETAILS

- Stereotaxic surgery
- *Ex vivo* electrophysiology and two-photon imaging
- Modeling
- Immunofluorescence
- Chemicals

- QUANTIFICATION AND STATISTICAL ANALYSIS

SUPPLEMENTAL INFORMATION

Supplemental information can be found online at https://doi.org/10.1016/j.celrep.2021.109483.

ACKNOWLEDGMENTS

We are grateful to Julie Hass and members of the Bender lab for assessing this work, the FamilieSCN2A Foundation for generous discussions, and Greg Hjelmstad for technical expertise in implementing dynamic clamp experiments. This work was supported by SFARI grants 513133 and 629287 (K.J.B.); the Natural Sciences and Engineering Research Council (NSERC) of Canada PGS-D Scholarship (P.W.E.S.); and NIH grants MH125978 (K.J.B.), NS095580 (R.B.-S.), and MH111662 (S.J.S.).

AUTHOR CONTRIBUTIONS

Conceptualization, P.W.E.S., R.B.-S., and K.J.B.; methodology, P.W.E.S., R.P.D.A., R.B.-S., A.S., H.K., C.M.K., and K.J.B.; software, P.W.E.S., R.B.-S., and H.K.; formal analysis, P.W.E.S. and K.J.B.; investigation, P.W.E.S., R.P.D.A., R.B.-S., A.S., H.K., C.M.K., and K.J.B.; resources, S.J.S. and K.J.B.; writing – original draft, P.W.E.S. and K.J.B.; writing – review & editing, all authors; visualization, P.W.E.S. and K.J.B.; supervision, K.J.B.; project administration, K.J.B.; funding acquisition, P.W.E.S., R.B.-S., S.J.S., and K.J.B.

DECLARATION OF INTERESTS

The authors declare no competing interests.

Received: February 9, 2021
Revised: May 17, 2021
Accepted: July 13, 2021
Published: August 3, 2021

REFERENCES

Azouz, R., and Gray, C.M. (2000). Dynamic spike threshold reveals a mechanism for synaptic coincidence detection in cortical neurons in vivo. Proc. Natl. Acad. Sci. USA *97*, 8110–8115.

Ben-Shalom, R., Keeshen, C.M., Berrios, K.N., An, J.Y., Sanders, S.J., and Bender, K.J. (2017). Opposing Effects on $Na_V1.2$ Function Underlie Differences Between SCN2A Variants Observed in Individuals With Autism Spectrum Disorder or Infantile Seizures. Biol. Psychiatry *82*, 224–232.

Bender, K.J., and Trussell, L.O. (2009). Axon initial segment Ca2+ channels influence action potential generation and timing. Neuron *61*, 259–271.

Brunklaus, A., Du, J., Steckler, F., Ghanty, I.I., Johannesen, K.M., Fenger, C.D., Schorge, S., Baez-Nieto, D., Wang, H.R., Allen, A., et al. (2020). Biological concepts in human sodium channel epilepsies and their relevance in clinical practice. Epilepsia *61*, 387–399.

Clarkson, R.L., Liptak, A.T., Gee, S.M., Sohal, V.S., and Bender, K.J. (2017). D3 Receptors Regulate Excitability in a Unique Class of Prefrontal Pyramidal Cells. J. Neurosci. *37*, 5846–5860.

Erisir, A., Lau, D., Rudy, B., and Leonard, C.S. (1999). Function of specific K(+) channels in sustained high-frequency firing of fast-spiking neocortical interneurons. J. Neurophysiol. *82*, 2476–2489.

Feng, Y.C.A., Howrigan, D.P., Abbott, L.E., Tashman, K., Cerrato, F., Singh, T., Heyne, H., Byrnes, A., Churchhouse, C., Watts, N., et al.; Epi25 Collaborative. Electronic address: s.berkovic@unimelb.edu.au; Epi25 Collaborative (2019). Ultra-Rare Genetic Variation in the Epilepsies: A Whole-Exome Sequencing Study of 17,606 Individuals. Am. J. Hum. Genet. *105*, 267–282.

Gaugler, T., Klei, L., Sanders, S.J., Bodea, C.A., Goldberg, A.P., Lee, A.B., Mahajan, M., Manaa, D., Pawitan, Y., Reichert, J., et al. (2014). Most genetic risk for autism resides with common variation. Nat. Genet. *46*, 881–885.

Gazina, E.V., Leaw, B.T.W., Richards, K.L., Wimmer, V.C., Kim, T.H., Aumann, T.D., Featherby, T.J., Churilov, L., Hammond, V.E., Reid, C.A., and Petrou, S. (2015). 'Neonatal' Nav1.2 reduces neuronal excitability and affects seizure susceptibility and behaviour. Hum. Mol. Genet. *24*, 1457–1468.

Goff, K.M., and Goldberg, E.M. (2019). Vasoactive intestinal peptide-expressing interneurons are impaired in a mouse model of Dravet syndrome. eLife *8*, e46846.

Gu, B., Shorter, J.R., Williams, L.H., Bell, T.A., Hock, P., Dalton, K.A., Pan, Y., Miller, D.R., Shaw, G.D., Philpot, B.D., and Pardo-Manuel de Villena, F. (2020). Collaborative Cross mice reveal extreme epilepsy phenotypes and genetic loci for seizure susceptibility. Epilepsia *61*, 2010–2021.

Guan, D., Tkatch, T., Surmeier, D.J., Armstrong, W.E., and Foehring, R.C. (2007). Kv2 subunits underlie slowly inactivating potassium current in rat neocortical pyramidal neurons. J. Physiol. *581*, 941–960.

Hallermann, S., de Kock, C.P.J., Stuart, G.J., and Kole, M.H.P. (2012). State and location dependence of action potential metabolic cost in cortical pyramidal neurons. Nat. Neurosci. *15*, 1007–1014.

Harnett, M.T., Xu, N.L., Magee, J.C., and Williams, S.R. (2013). Potassium channels control the interaction between active dendritic integration compartments in layer 5 cortical pyramidal neurons. Neuron *79*, 516–529.

Hay, E., Hill, S., Schürmann, F., Markram, H., and Segev, I. (2011). Models of neocortical layer 5b pyramidal cells capturing a wide range of dendritic and perisomatic active properties. PLoS Comput. Biol. *7*, e1002107.

Howell, K.B., McMahon, J.M., Carvill, G.L., Tambunan, D., Mackay, M.T., Rodriguez-Casero, V., Webster, R., Clark, D., Freeman, J.L., Calvert, S., et al. (2015). SCN2A encephalopathy: A major cause of epilepsy of infancy with migrating focal seizures. Neurology *85*, 958–966.

Hu, W., Tian, C., Li, T., Yang, M., Hou, H., and Shu, Y. (2009). Distinct contributions of Na(v)1.6 and Na(v)1.2 in action potential initiation and backpropagation. Nat. Neurosci. *12*, 996–1002.

Jenerick, H. (1963). Phase Plane Trajectories of the Muscle Spike Potential. Biophys. J. *3*, 363–377.

Kaczmarek, L.K., and Zhang, Y. (2017). Kv3 channels: Enablers of rapid firing, neurotransmitter release, and neuronal endurance. Physiol. Rev. *97*, 1431–1468.

Kang, S.K., Hawkins, N.A., and Kearney, J.A. (2018). C57BL/6J and C57BL/6N substrains differentially influence phenotype severity in the *Scn1a* $^{+/-}$ mouse model of Dravet syndrome. Epilepsia Open *4*, 164–169.

Katz, E., Stoler, O., Scheller, A., Khrapunsky, Y., Goebbels, S., Kirchhoff, F., Gutnick, M.J., Wolf, F., and Fleidervish, I.A. (2018). Role of sodium channel subtype in action potential generation by neocortical pyramidal neurons. Proc. Natl. Acad. Sci. USA *115*, E7184–E7192.

Kole, M.H.P., Letzkus, J.J., and Stuart, G.J. (2007). Axon initial segment Kv1 channels control axonal action potential waveform and synaptic efficacy. Neuron *55*, 633–647.

Korngreen, A., and Sakmann, B. (2000). Voltage-gated K+ channels in layer 5 neocortical pyramidal neurones from young rats: subtypes and gradients. J. Physiol. *525*, 621–639.

Lau, D., Vega-Saenz de Miera, E.C., Contreras, D., Ozaita, A., Harvey, M., Chow, A., Noebels, J.L., Paylor, R., Morgan, J.I., Leonard, C.S., and Rudy, B. (2000). Impaired fast-spiking, suppressed cortical inhibition, and increased susceptibility to seizures in mice lacking Kv3.2 K+ channel proteins. J. Neurosci. *20*, 9071–9085.

Leu, C., Stevelink, R., Smith, A.W., Goleva, S.B., Kanai, M., Ferguson, L., Campbell, C., Kamatani, Y., Okada, Y., Sisodiya, S.M., et al.; Epi25

Consortium (2019). Polygenic burden in focal and generalized epilepsies. Brain *142*, 3473–3481.

Li, T., Tian, C., Scalmani, P., Frassoni, C., Mantegazza, M., Wang, Y., Yang, M., Wu, S., and Shu, Y. (2014). Action potential initiation in neocortical inhibitory interneurons. PLoS Biol. *12*, e1001944.

Li, M., Jancovski, N., Jafar-Nejad, P., Burbano, L.E., Rollo, B., Richards, K., Drew, L., Sedo, A., Pachernegg, S., Soriano, A., et al. (2020). Antisense oligonucleotide therapy for SCN2A gain-of-function epilepsy. BioRxiv, 2020.09.09.289900.

Lopez-Santiago, L.F., Yuan, Y., Wagnon, J.L., Hull, J.M., Frasier, C.R., O'Malley, H.A., Meisler, M.H., and Isom, L.L. (2017). Neuronal hyperexcitability in a mouse model of *SCN8A* epileptic encephalopathy. Proc. Natl. Acad. Sci. USA *114*, 2383–2388.

Macica, C.M., von Hehn, C.A.A., Wang, L.Y., Ho, C.S., Yokoyama, S., Joho, R.H., and Kaczmarek, L.K. (2003). Modulation of the kv3.1b potassium channel isoform adjusts the fidelity of the firing pattern of auditory neurons. J. Neurosci. *23*, 1133–1141.

Makinson, C.D., Tanaka, B.S., Sorokin, J.M., Wong, J.C., Christian, C.A., Goldin, A.L., Escayg, A., and Huguenard, J.R. (2017). Regulation of Thalamic and Cortical Network Synchrony by Scn8a. Neuron *93*, 1165–1179.e6.

Markram, H., Muller, E., Ramaswamy, S., Reimann, M.W., Abdellah, M., Sanchez, C.A., Ailamaki, A., Alonso-Nanclares, L., Antille, N., Arsever, S., et al. (2015). Reconstruction and Simulation of Neocortical Microcircuitry. Cell *163*, 456–492.

Martin, M.S., Dutt, K., Papale, L.A., Dubé, C.M., Dutton, S.B., de Haan, G., Shankar, A., Tufik, S., Meisler, M.H., Baram, T.Z., et al. (2010). Altered function of the SCN1A voltage-gated sodium channel leads to γ-aminobutyric acid-ergic (GABAergic) interneuron abnormalities. J. Biol. Chem. *285*, 9823–9834.

Mishra, V., Karumuri, B.K., Gautier, N.M., Liu, R., Hutson, T.N., Vanhoof-Villalba, S.L., Vlachos, I., Iasemidis, L., and Glasscock, E. (2017). Scn2a deletion improves survival and brain-heart dynamics in the Kcna1-null mouse model of sudden unexpected death in epilepsy (SUDEP). Hum. Mol. Genet. *26*, 2091–2103.

Miyamoto, H., Tatsukawa, T., Shimohata, A., Yamagata, T., Suzuki, T., Amano, K., Mazaki, E., Raveau, M., Ogiwara, I., Oba-Asaka, A., et al. (2019). Impaired cortico-striatal excitatory transmission triggers epilepsy. Nat. Commun. *10*, 1917.

Niday, Z., and Tzingounis, A.V. (2018). Potassium Channel Gain of Function in Epilepsy: An Unresolved Paradox. Neuroscientist *24*, 368–380.

Ogiwara, I., Miyamoto, H., Morita, N., Atapour, N., Mazaki, E., Inoue, I., Takeuchi, T., Itohara, S., Yanagawa, Y., Obata, K., et al. (2007). Nav1.1 localizes to axons of parvalbumin-positive inhibitory interneurons: a circuit basis for epileptic seizures in mice carrying an Scn1a gene mutation. J. Neurosci. *27*, 5903–5914.

Ogiwara, I., Miyamoto, H., Tatsukawa, T., Yamagata, T., Nakayama, T., Atapour, N., Miura, E., Mazaki, E., Ernst, S.J., Cao, D., et al. (2018). Nav1.2 haploinsufficiency in excitatory neurons causes absence-like seizures in mice. Commun. Biol. *1*, 96.

Planells-Cases, R., Caprini, M., Zhang, J., Rockenstein, E.M., Rivera, R.R., Murre, C., Masliah, E., and Montal, M. (2000). Neuronal death and perinatal lethality in voltage-gated sodium channel α(II)-deficient mice. Biophys. J. *78*, 2878–2891.

Poolos, N.P., and Johnston, D. (2012). Dendritic ion channelopathy in acquired epilepsy. Epilepsia *53*, 32–40.

Ramaswamy, S., and Markram, H. (2015). Anatomy and physiology of the thick-tufted layer 5 pyramidal neuron. Front. Cell. Neurosci. *9*, 233.

Sanders, S.J., Campbell, A.J., Cottrell, J.R., Moller, R.S., Wagner, F.F., Auldridge, A.L., Bernier, R.A., Catterall, W.A., Chung, W.K., Empfield, J.R., et al. (2018). Progress in Understanding and Treating SCN2A-Mediated Disorders. Trends Neurosci. *41*, 442–456.

Shin, W., Kweon, H., Kang, R., Kim, D., Kim, K., Kang, M., Kim, S.Y., Hwang, S.N., Kim, J.Y., Yang, E., et al. (2019). Scn2a haploinsufficiency in mice suppresses hippocampal neuronal excitability, excitatory synaptic drive, and long-term potentiation, and spatial learning and memory. Front. Mol. Neurosci. *12*, 145.

Speed, D., O'Brien, T.J., Palotie, A., Shkura, K., Marson, A.G., Balding, D.J., and Johnson, M.R. (2014). Describing the genetic architecture of epilepsy through heritability analysis. Brain *137*, 2680–2689.

Spratt, P.W.E., Ben-Shalom, R., Keeshen, C.M., Burke, K.J., Jr., Clarkson, R.L., Sanders, S.J., and Bender, K.J. (2019). The Autism-Associated Gene Scn2a Contributes to Dendritic Excitability and Synaptic Function in the Prefrontal Cortex. Neuron *103*, 673–685.e5.

Taddese, A., and Bean, B.P. (2002). Subthreshold sodium current from rapidly inactivating sodium channels drives spontaneous firing of tuberomammillary neurons. Neuron *33*, 587–600.

Tai, C., Abe, Y., Westenbroek, R.E., Scheuer, T., and Catterall, W.A. (2014). Impaired excitability of somatostatin- and parvalbumin-expressing cortical interneurons in a mouse model of Dravet syndrome. Proc. Natl. Acad. Sci. U.S.A. *11*, E3139–E3148.

Thompson, C.H., Ben-Shalom, R., Bender, K.J., and George, A.L. (2020). Alternative splicing potentiates dysfunction of early-onset epileptic encephalopathy SCN2A variants. J. Gen. Physiol. *152*, e201912442.

Uebachs, M., Schaub, C., Perez-Reyes, E., and Beck, H. (2006). T-type Ca^{2+} channels encode prior neuronal activity as modulated recovery rates. J. Physiol. *571*, 519–536.

Williams, S.R., and Mitchell, S.J. (2008). Direct measurement of somatic voltage clamp errors in central neurons. Nat. Neurosci. *11*, 790–798.

Wolff, M., Johannesen, K.M., Hedrich, U.B.S., Masnada, S., Rubboli, G., Gardella, E., Lesca, G., Ville, D., Milh, M., Villard, L., et al. (2017). Genetic and phenotypic heterogeneity suggest therapeutic implications in SCN2A-related disorders. Brain *140*, 1316–1336.

Zagha, E., Lang, E.J., and Rudy, B. (2008). Kv3.3 channels at the Purkinje cell soma are necessary for generation of the classical complex spike waveform. J. Neurosci. *28*, 1291–1300.

Zhang, J., Chen, X., Eaton, M., Lai, S., Park, A., Ahmad, T.S., Wu, J., Ma, Z., Que, Z., Hea Lee, J., et al. (2021). Severe deficiency of the voltage-gated sodium channel $Na_V1.2$ elevates neuronal excitability in adult mice. Cell Rep. *36*. https://doi.org/10.1016/j.celrep.2021.109495.

STAR★METHODS

KEY RESOURCES TABLE

REAGENT or RESOURCE	SOURCE	IDENTIFIER
Antibodies		
Rabbit IgG Anti-$Na_V1.6$	Alomone	ASC-009, RRID:AB_2040202
rabbit IgG Anti-$Na_V1.2$	Abcam	ab65163, RRID:AB_2254204
mouse IgG2a Anti-ankyrin-G	Neuromab	75-146, RRID:AB_10673030
Alexa Fluor 488-conjugated goat anti-rabbit IgG	Thermo Fisher Scientific	A11070
Alexa Fluor 647-conjugated goat anti-mouse igG2a	Thermo Fisher Scientific	A21241
Bacterial and virus strains		
AAV5-Ef1α-Cre-mCherry	UNC Viral Core	N/A
Chemicals, peptides, and recombinant proteins		
NBQX disodium salt	Tocris	0373
Tetrodotoxin-citrate	Alomone	T-550
(*R*)-CPP	Tocris	0247
Picrotoxin	Tocris	1128
Fluo-5F, Pentapotassium Salt, cell impermeant	Invitrogen	F14221
Alexa Fluor 594 hydrazide	Invitrogen	A10438
Prolong Gold Antifade with DAPI	Life Technologies	P36941
Experimental models: Organisms/strains		
Mouse: Ai14: 6;129S6-*Gt(ROSA)26Sor*$^{tm14(CAG-tdTomato)Hze}$/J	The Jackson Laboratory	JAX: 007908
Mouse: C57B6J	The Jackson Laboratory	JAX: 000664
Mouse: *Scn2a*$^{+/-}$	M. Montal / E. Glasscock	PMID: 10827969, 28334922
Mouse: *Scn2a*$^{+/fl}$	Bender lab	PMID: 31230762
Software and algorithms		
IGOR Pro	Wavemetrics	RRID:SCR_000325; v6.3
FIJI	https://fiji.sc/	RRID:SCR_002285
MATLAB	Mathworks	RRID:SCR_001622; v2016a
Python	python.org	RRID:SCR_008394 ; v3.5.2
Compartmental Models	This manuscript, modelDB	Access Number: 267067 https://modeldb.yale.edu/267067

RESOURCE AVAILABILITY

Lead contact

Further information and requests for resources and reagents should be directed to and will be fulfilled by the Lead Contact, Kevin Bender (kevin.bender@ucsf.edu).

Materials availability

All unique/stable reagents generated in this study are available from the Lead Contact with a completed Materials Transfer Agreement.

Data and code availability

Data: Data reported in this paper will be shared by the lead contact upon reasonable request.

Code: All original code describing compartmental models implemented herein has been deposited at modelDB and is publicly available as of the date of publication. The access number is listed in the Key resources table.

Any additional information required to reanalyze the data reported in this paper is available from the lead contact upon request.

EXPERIMENTAL MODEL AND SUBJECT DETAILS

All experimental procedures were performed in accordance with UCSF IACUC guidelines. All experiments were performed on mice housed under standard conditions with *ad libitum* access to food and water. C57B6J (JAX: 000664) were obtained from The Jackson Laboratory and used for backcrossing of all mouse strains. *Scn2a*$^{+/-}$ mice were provided by Drs. E. Glasscock and M. Montal (Mishra et al., 2017; Planells-Cases et al., 2000). *Scn2a*$^{+/fl}$ mice were created as described previously (Spratt et al., 2019). Male and female mice were used throughout, with ages noted below.

METHOD DETAILS

Stereotaxic surgery

Mice were anesthetized with isoflurane and positioned in a stereotaxic apparatus. 500 nL volumes of AAV-EF1A-Cre-IRES-mCherry (UNC Vector Core)) were injected into the mPFC of *Scn2a*$^{+/+}$, *Scn2a*$^{fl/+}$ and *Scn2a*$^{fl/fl}$ mice (stereotaxic coordinates [mm]: anterior-posterior [AP], +1.7, mediolateral [ML] −0.35; dorsoventral [DV]: −2.6). Mice were used in experiments four to eight weeks post injection.

Ex vivo electrophysiology and two-photon imaging

Two-photon imaging and current- and voltage-clamp electrophysiology were performed as described previously (Spratt et al., 2019). Briefly, mice at postnatal day 56-104 were anesthetized and 250 μm-thick coronal slices containing medial prefrontal cortex were prepared. Slices were prepared from *Scn2a*$^{+/-}$, *Scn2a*$^{+/fl}$, Scn2a$^{fl/fl}$, or *Scn2a* wild-type littermates (genotyped by PCR). All data were acquired and analyzed blind to *Scn2a* genotype. Data were acquired from both sexes (blind to sex). Cutting solution contained (in mM): 87 NaCl, 25 $NaHCO_3$, 25 glucose, 75 sucrose, 2.5 KCl, 1.25 NaH_2PO_4, 0.5 $CaCl_2$ and 7 $MgCl_2$; bubbled with 5%CO_2/95%O_2; 4°C. Following cutting, slices were incubated in the same solution for 30 min at 33°C, then at room temperature until recording. Recording solution contained (in mM): 125 NaCl, 2.5 KCl, 2 $CaCl_2$, 1 $MgCl_2$, 25 $NaHCO_3$, 1.25 NaH_2PO_4, 25 glucose; bubbled with 5%CO_2/95%O_2; 32-34°C, ~310 mOsm.

Neurons were visualized with Dodt-contrast optics for conventional visually guided whole-cell recording, or with 2-photon-guided imaging of reporter-driven tdTomato fluorescence overlaid on an image of the slice (scanning DIC). For current-clamp recordings and voltage-clamp recordings of K^+ currents, patch electrodes (Schott 8250 glass, 3-4 MΩ tip resistance) were filled with a solution containing (in mM): 113 K-Gluconate, 9 HEPES, 4.5 $MgCl_2$, 0.1 EGTA, 14 $Tris_2$-phosphocreatine, 4 Na_2-ATP, 0.3 tris-GTP; ~290 mOsm, pH: 7.2-7.25. For Ca^{2+} imaging, EGTA was replaced with 250 μM Fluo-5F and 20 μM Alexa 594. For voltage-clamp recordings of persistent Na^+ currents, internal solution contained (in mM): 110 $CsMeSO_3$, 40 HEPES, 1 KCl, 4 NaCl, 4 Mg-ATP, 10 Na-phosphocreatine, 0.4 Na_2-GTP, 0.1 EGTA; ~290 mOsm, pH: 7.22. All data were corrected for measured junction potentials of 12 and 11 mV in K- and Cs-based internals, respectively.

Electrophysiological data were acquired using Multiclamp 700A or 700B amplifiers (Molecular Devices) via custom routines in Igor-Pro (Wavemetrics) from layer 5b thick tufted neurons, using metrics as previously described (Spratt et al., 2019). Data were acquired at 50 kHz and filtered at 20 kHz. For current-clamp recordings, pipette capacitance was compensated by 50% of the fast capacitance measured under gigaohm seal conditions in voltage-clamp prior to establishing a whole-cell configuration, and the bridge was balanced. For voltage-clamp recordings, pipette capacitance was compensated completely, and series resistance was compensated 50%. Series resistance was < 15 MΩ in all recordings. Experiments were omitted if input resistance changed by > ± 15%. AP threshold and peak dV/dt measurements were determined from the first AP evoked by a near-rheobase current in pyramidal cells (300 ms duration; 10 pA increments), or the first AP within a train of APs with a minimum inter-AP frequency of 25 Hz in inhibitory neurons. Threshold was defined as the V_m when dV/dt measurements first exceeded 15 V/s. AHPs were defined as the minimum voltage between APs.

Persistent Na^+ and currents were activated with 500 ms voltage steps from −90 mV. 10-15 trials were averaged per voltage step. Current amplitudes were calculated as the average of the last 100 ms of each step. Experiments were performed in 25 μM picrotoxin, 10 μM NBQX, 10 mM TEA, 2 mM 4-AP, 200 μM Cd^{2+}, 2 μM TTA-P2, and 1 mM Cs^+. Whole-cell K^+ currents were activated with 500 ms voltage steps from −90 to −20 mV, in 10 mV increments. 5 trials were averaged per voltage step. Current amplitudes were calculated from the transient peak and sustained components (last 50 ms). Experiments were performed in 500 nM TTX, 25 μM picrotoxin, 10 μM NBQX, and 1 mM Cs^+. Ca^{2+} channels were not blocked to allow for activation of Ca^{2+}-dependent K^+ channels. Nucleated K+ currents were activated with 500 ms voltage steps from −100 to +30 mV in 10 mV increments. 2 trails were averaged per voltage step. Delayed onset currents were isolated with a 100 ms pre-pulse to −50 mV. Transient K+ currents were isolated by subtracting delayed currents from total current. Data were normalized to total membrane capacitance. Leak currents were subtracted in all voltage-clamp data using p/n leak subtraction. Conductance-voltage plots of both transient and delayed K^+ responses were fit with Boltzmann functions to extract voltage at half-maximum ($V_{1/2}$).

Dynamic clamp experiments were performed using a dPatch amplifier (Sutter Instrument) with identical internal and external solutions as in current-clamp experiments. For these experiments, pipettes were wrapped with parafilm to reduce pipette capacitance to 7.2 ± 0.1 pF, and capacitance was compensated to 90% of values obtained when establishing gigaohm seals. Series resistance (6.6 ± 0.2 MΩ) was bridge balanced completely. Data were acquired at 100-200 kHz and low pass filtered at 10-20 kHz. $Na_V1.2$ was

simulated with an 8 state Markov model from Hallermann et al. (2012), $K_{transient}$ was modeled based on nucleated-patch recordings from neocortical pyramidal cells (Korngreen and Sakmann, 2000). $K_{transient}$ and $K_{delayed}$ were simulated with the "K_t" "K_m" Hodgkin Huxley-based models from Hay et al. (2011). In all cases, a voltage offset variable was added to account for junction potential offsets. Control trials without conductance injection were interleaved on a trial by trial basis in all experiments.

Modeling

A pyramidal cell compartmental model was implemented in the NEURON environment (v7.5), based on a Blue Brain Project model of a thick-tufted layer 5b pyramidal cell (TTPC1) (Markram et al., 2015; Ramaswamy and Markram, 2015). The TTPC1 model was adjusted to include an AIS and Na channels in the TTPC1 model were replaced with $Na_V1.2$ and $Na_V1.6$ channels in compartments and densities as described previously (Ben-Shalom et al., 2017). For phase plane comparisons, the first AP evoked with 500 pA stimulus intensity (25 ms duration) were compared in each model configuration, with threshold considered the membrane potential when dV/dt exceeds 15 V/s.

Immunofluorescence

Tissue samples were collected from P60-90 *Scn2a*$^{fl/fl}$ mice stereotaxically injected with pAAV-Ef1a-mcherry-IRES-Cre unilaterally into mPFC after intracardiac perfusion with 4% paraformaldehyde in phosphate buffered saline (PBS). The tissue was then fixed in 4% paraformaldehyde for 2 hours and cryopreserved in increasing concentrations of sucrose in PBS (15% then 30%) overnight at 4°C. Tissue samples were embedded at −80°C in Tissue-Tek O.C.T compound and sectioned coronally into 30-μm thick sections on a cryostat. Sections were rinsed in PBS and then blocked with 10% normal goat serum with 0.2% Triton X-100 in PBS for 40 minutes at room temperature. Sections were incubated overnight with primary antibodies diluted in 0.1% Triton X-100 in PBS with 2% normal goat serum at 4°C. Primary antibodies were as follows: Rabbit IgG Anti-$Na_V1.6$ (Alomone ASC-009; 1:200), rabbit IgG Anti-$Na_V1.2$ (Abcam ab65163; 1:250), mouse IgG2a Anti-ankyrin-G (Neuromab 75-146; 1:500). Sections were then rinsed in PBS and incubated for 2 hours in secondary antibodies diluted in 0.1% Triton X-100 in PBS with 2% normal goat serum at room temperature. Secondary antibodies were Alexa Fluor 488-conjugated goat anti-rabbit IgG (1:500; A11070, Thermo Fisher Scientific), and Alexa Fluor 647-conjugated goat anti-mouse igG2a (1:500; A21241, Thermo Fisher Scientific). Sections were then rinsed in PBS and slides were mounted with ProLong Gold Antifade mounting media with DAPI (P36931, Thermo Fisher Scientific) and stored at 4°C until imaging.

Images were collected on a Fluoview3000 (Olympus) using appropriate bandpass filters with a 40x 1.4 NA objective with laser intensities and photomultiplier voltages held constant across sections. Serial z stacks were acquired at 0.1 μm steps in Z, with XY zoom adjusted to 2x Nyquist resolution. Data were stitched using proprietary Olympus software with no adjustment of pixel intensities near borders between stacks. Fluorescent intensity in the AIS was analyzed using image-J by manually drawing a region of interest around the AIS using ankyrin-G labeling as a guide (Na_V channel was not visible to the experimentalist). Average pixel intensity was then calculated within this region for Na_V and ankyrin-G channels. Analysis was limited to PFC layer 5b using established layer divisions (Clarkson et al., 2017). $Na_V1.6$ intensity was normalized to the average ankyrin-G intensity per section to control for variability across animals. $Na_V1.2$ staining in the AIS, which was associated with a higher level of diffuse neuropil staining than $Na_V1.6$, was first background subtracted from regions of interest of identical size and shape immediately adjacent to each AIS, then normalized to ankyrin-G intensity.

Chemicals

Fluo-5F pentapotassium salt and Alexa Fluor 594 hydrazide Na^+ salt were from Invitrogen. Picrotoxin, R-CPP, and NBQX were from Tocris. TTX-citrate was from Alomone. All others were from Sigma.

QUANTIFICATION AND STATISTICAL ANALYSIS

Data are summarized either with boxplots depicting the median, quartiles, and 90% tails, with violin plots with individual datapoints overlaid, or with mean ± standard error. n denotes cells for all electrophysiology. Data were obtained from 4-14 mice per condition for electrophysiology and imaging experiments. Group sample sizes were chosen based on standards in the field, and no statistical methods were used to predetermine sample size. Unless specifically noted, no assumptions were made about the underlying distributions of the data and two-sided, rank-based nonparametric tests were used. Statistical tests are noted throughout text. Significance was set at an alpha value of 0.05, with a Bonferroni correction for multiple comparisons when appropriate. Statistical analysis was performed using Statview (SAS), and custom routines in MATLAB R2016b (Mathworks), and Python 3.6.4.

Cell Reports, Volume *36*

Supplemental information

Paradoxical hyperexcitability from $Na_V1.2$ sodium channel loss in neocortical pyramidal cells

Perry W.E. Spratt, Ryan P.D. Alexander, Roy Ben-Shalom, Atehsa Sahagun, Henry Kyoung, Caroline M. Keeshen, Stephan J. Sanders, and Kevin J. Bender

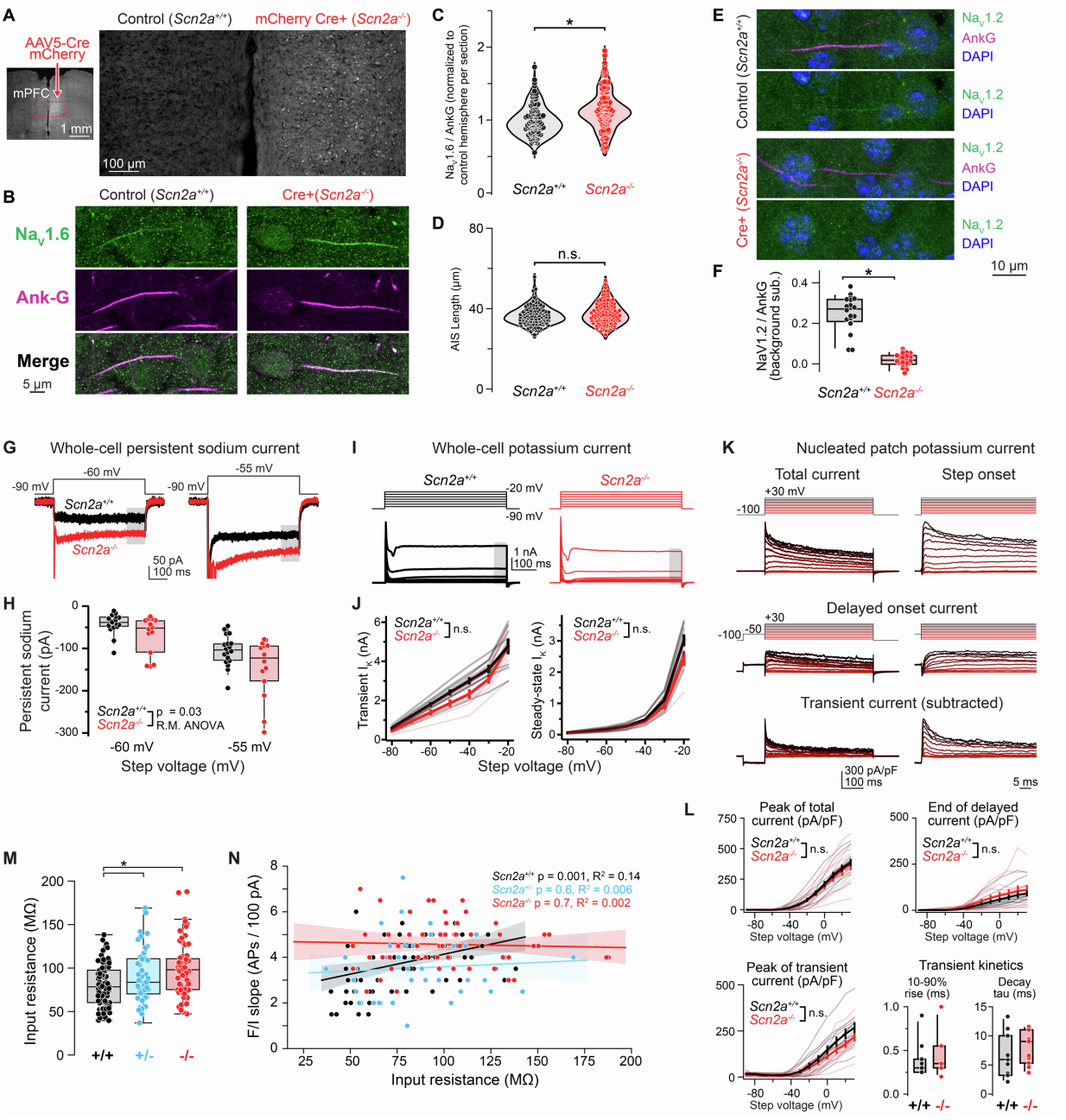

Figure S1, related to Fig. 1: Currents and intrinsic properties of *Scn2a*$^{-/-}$ cells

A: Example injection of unilateral AAV5-mCherry-Cre into mPFC of mouse at P28. Comparisons were made between injected (*Scn2a*$^{-/-}$) and control (*Scn2a*$^{+/+}$) hemispheres. Scale bars are 1 mm and 100 µm.

B: Immunostaining of $Na_V1.6$ and ankyrin-G in layer 5 of both hemispheres. Scale:5 µm.

C: Quantification of $Na_V1.6$ staining. Intensity in each AIS was normalized to ankyrin-G. Data were then normalized to mean ankyrin-G intensity of all initial segments analyzed within each section (both hemispheres). Data plotted as violin plots with individual initial segments as single points. *: $p < 0.001$, Mann-Whitney. n = 126 WT and 123 *Scn2a*$^{-/-}$ initial segments across 3 animals.

D: AIS length was not altered by $Na_V1.2$ knockout ($p = 0.14$, Mann-Whitney).

E: Immunostaining of $Na_V1.2$ and ankyrin-G in both hemispheres. Scale: 10 μm.

F: Quantification of $Na_V1.2$ staining. n = 20 WT, 24 *Scn2a*$^{-/-}$; *: $p < 0.0001$, Mann-Whitney. $Na_V1.2$ intensity is not different than 0 ($p = 0.07$, one sample t-test). Box plots in F, H, M, L are medians and quartiles with 90% tails.

G: Example persistent sodium currents from *Scn2a*$^{+/+}$ (black) and *Scn2a*$^{-/-}$ (red) cells for voltage steps from -90 to -60 or -55 mV.

H: Summary of persistent currents for each voltage step. $p = 0.03$, repeated measures ANOVA across genotypes. n = 18 WT, 14 *Scn2a*$^{-/-}$ cells.

I: Example whole-cell potassium currents from *Scn2a*$^{+/+}$ (black) and *Scn2a*$^{-/-}$ (red) cells for voltage steps from -90 to -20 mV in 10 mV increments.

J: Summary for transient onset current and steady state current (last 50 ms before voltage step offset, grey area in I). Thick lines and bars are mean ± SEM across population. Light, thin lines are data from single cells (n = 11 WT, 10 *Scn2a*$^{-/-}$ cells). Data analyzed with repeated measures ANOVA.

K: Example nucleated patch potassium currents for voltage steps from -100 to +30 mV (color coded from red to black for increasing step amplitude). Total current for 500 ms step and highlight of step onset are shown. Delayed onset currents measured following 100 ms prepulse to -50 mV; transient currents were calculated by subtracting delayed onset current from total current. All currents normalized to patch capacitance.

L: Summary for peak of total current (at onset), the last 50 ms of the delayed current, the peak of the transient current (onset), and the kinetics of the transient current. Amplitudes shown and analyzed as in J; Kinetics analyzed with Mann-Whitney statistics. n = 11 WT, 11 *Scn2a*$^{-/-}$ cells.

M: Input resistance for all cells in Fig. 1. *: $p < 0.001$, Kruskall-Wallis test, Wilcoxon rank sum posthoc test. n = 77 WT, 40 *Scn2a*$^{+/-}$, 60 *Scn2a*$^{-/-}$ cells.

N: Input resistance vs. the slope of the F/I curve between 100 and 300 pA for each cell. Data color-coded as in K. Lines and shaded regions represent best linear fit and 95% confidence intervals. p and R2 values noted in figure. n = 77 WT, 40 *Scn2a*$^{+/-}$, 60 *Scn2a*$^{-/-}$ cells.

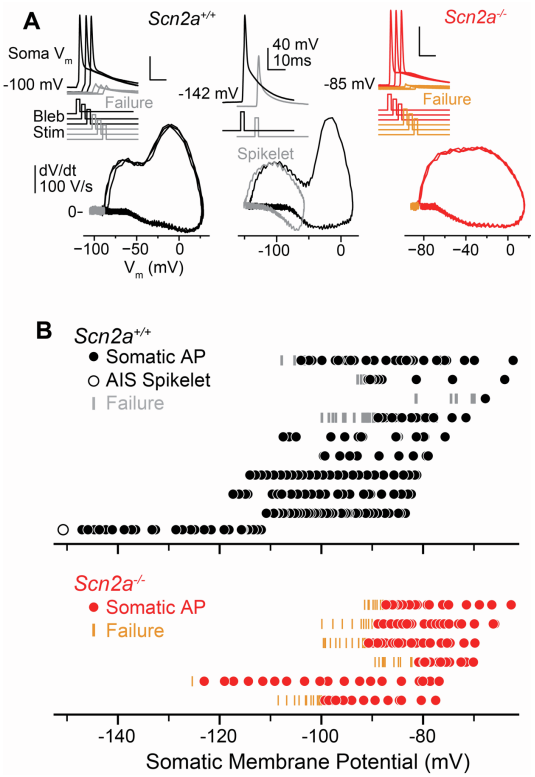

Figure S2, related to Fig. 2: Somatic invasion of APs initiated from axonal bleb

A: Examples of successive single APs evoked with 2 ms, 2 nA current injection at bleb. Somatic V_m was hyperpolarized on successive trials with steps of somatic bias current, eventually hyperpolarizing to the point that no APs could be evoked via bleb current injection. Bleb stim timing offset for clarity. Similar effects noted in WT and *Scn2a*$^{-/-}$ cells. Spikelet observed once at -150 mV in WT cell (middle). Note differences in X scale for each phase-plane.

B: Summary across all WT and *Scn2a*$^{-/-}$ cells. Each row is a single cell, with somatic AP successes, failures, and spikelets at each somatic voltage plotted as closed circles, vertical lines, and open circles, respectively. n = 10 WT and 6 *Scn2a*$^{-/-}$ cells.

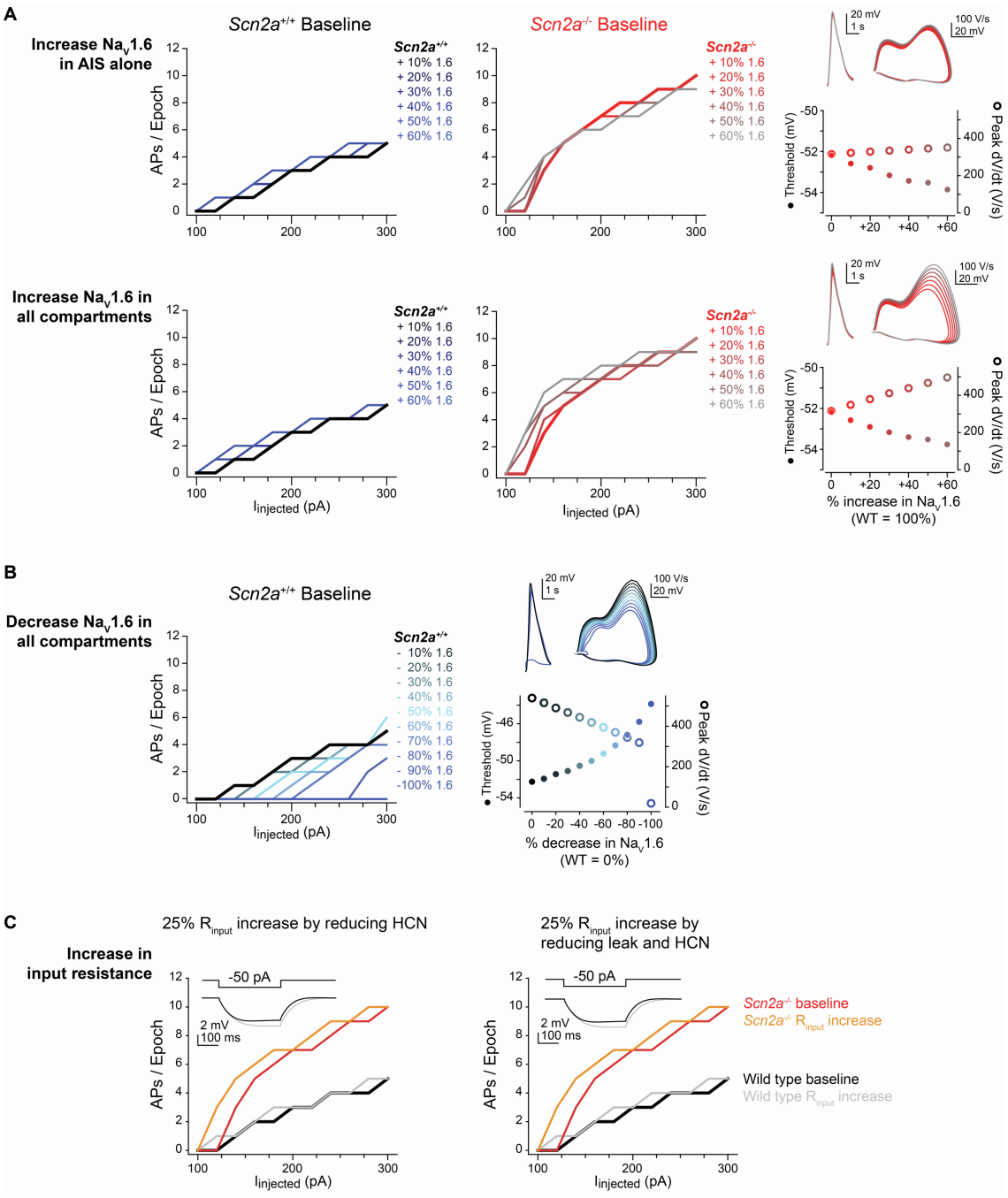

Figure S3, related to Fig. 3: Altering $Na_V1.6$ density or increasing input resistance in models do not recapitulate empirical results.

A: Increased $Na_V1.6$ density (10% increments over baseline levels in each compartment) either in the AIS alone (top row, matching immunofluorescence and persistent current observations) or in all compartments (bottom row, assuming similar effects as those observed in AIS) has minimal effect on F/I curves in WT models (left, blue), or in *Scn2a*$^{-/-}$ models (right, red). Note that, in both cases, AP threshold hyperpolarizes with increased $Na_V1.6$ density, an effect not observed *ex vivo* (Fig. 1).

B: Decreased $Na_V1.6$ density (10% increments from baseline WT levels to full knockout, all compartments) increases AP threshold and reduces F/I curve. Contrast with $Na_V1.2$ knockout (Fig. 3).

C: Increases in input resistance, mimicking ~25% increases observed in empirical data (Fig. S1), were modeled by reducing HCN channel density alone (left), as these channels are principal contributors to input resistance in thick tufted pyramidal cells (Dembrow et al., 2010), or by reducing leak current to zero and additionally reducing HCN channel density (right, as elimination of leak currents alone cannot increase input resistance by 25%). Different input resistance configurations were modeled in wild type and *Scn2a*$^{-/-}$ cells. Note that increased input resistance shifts the onset of the F/I curve left, an effect not observed in empirical data. Furthermore, increasing input resistance alone does not evoke marked increases in excitability.

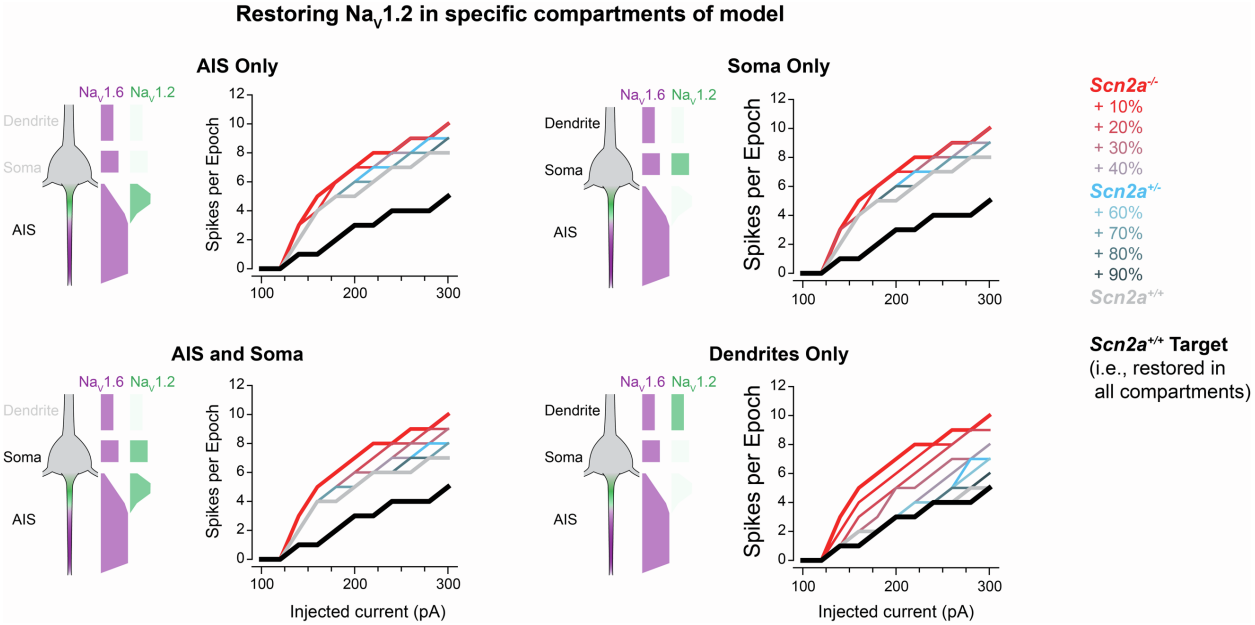

Figure S4, related to Fig. 4: Limitations in space-clamp of injected conductances prevents full restoration of *Scn2a*$^{+/+}$-like F/I curves in *Scn2a*$^{-/-}$ cells.

Compartmental models in which Na$_V$1.2 density was progressively restored from *Scn2a*$^{-/-}$ to *Scn2a*$^{+/+}$ levels (10% increments) in specific compartments. Data compared to "target" of complete restoration in all compartments (black: AIS, soma, dendrite). Note difficulty separating *Scn2a*$^{-/-}$ curve from 80% restoration curve in AIS or soma-only conditions.